

## THE BISPECTRUM OF REDSHIFTED 21-CM FLUCTUATIONS FROM THE DARK AGES

ANNALISA PILLEPICH<sup>1</sup>, CRISTIANO PORCIANI<sup>1</sup> AND SABINO MATARRESE<sup>2</sup>

## Abstract

Brightness-temperature fluctuations in the redshifted 21-cm background from the cosmic dark ages are generated by irregularities in the gas-density distribution and can then be used to determine the statistical properties of density fluctuations in the early Universe. We first derive the most general expansion of brightness-temperature fluctuations up to second order in terms of all the possible sources of spatial fluctuations. We then focus on the three-point statistics and compute the angular bispectrum of brightness-temperature fluctuations generated prior to the epoch of hydrogen reionization. For simplicity, we neglect redshift-space distortions. We find that low-frequency radio experiments with arcmin angular resolution can easily detect non-Gaussianity produced by non-linear gravity with high signal-to-noise ratio. The bispectrum thus provides a unique test of the gravitational instability scenario for structure formation, and can be used to measure the cosmological parameters. Detecting the signature of primordial non-Gaussianity produced during or right after an inflationary period is more challenging but still possible. An ideal experiment limited by cosmic variance only and with an angular resolution of a few arcsec has the potential to detect primordial non-Gaussianity with a non-linearity parameter of  $f_{\text{NL}} \sim 1$ . Additional sources of error as weak lensing and an imperfect foreground subtraction could severely hamper the detection of primordial non-Gaussianity which will benefit from the use of optimal estimators combined with tomographic techniques.

*Subject headings:* cosmology: theory – diffuse radiation – intergalactic medium

## 1. INTRODUCTION

During the dark ages (the time between recombination and the formation of the first stars), the cosmic microwave background (CMB) is coupled to atoms of neutral hydrogen through spin-flip 21-cm transitions. Due to the resonant nature of the interaction, neutral hydrogen at redshift  $z$  imprints a signature at a wavelength of  $21.12(1+z)$  cm in the CMB. The brightness temperature of the CMB at radio wavelengths thus probes the three-dimensional neutral hydrogen distribution at  $30 < z < 100$ . This accurately traces dark-matter inhomogeneities down to the Jeans length ( $\sim 10$  comoving pc corresponding to angular separations of  $\sim 10^{-2}$  arcsec). On smaller scales, the finite pressure of the gas keeps the baryons uniformly distributed. The expected power-spectrum of fluctuations in the 21-cm background from the dark ages has been recently calculated (Loeb & Zaldarriaga 2004; Bharadwaj & Ali 2004). In this paper, we focus on the three-point statistics. In particular, we compute the bispectrum of 21-cm maps. This is obtained by expanding the brightness temperature of the cosmic background up to second order in the underlying density fluctuations. Related work has been presented by Cooray (2005) who discussed the large-scale non-Gaussianity generated during the era of reionization and by Saiyad, Bharadwaj & Pandey (2006) who focussed on the post-reionization era ( $z < 6$ ).

Measuring the bispectrum of fluctuations in the 21-cm background will ultimately allow to quantify the degree of non-Gaussianity (NG) of the dark matter density field at high-redshift. Such a non-Gaussianity has two possible origins: non-linearity due to the usual Newtonian gravitational instability and non-Gaussianity which is intrinsic in the mechanism generating the primordial seeds, i.e. arising during or immediately after inflation, as well as post-Newtonian terms inherent in the solution of Einstein's equations to second order (Bartolo, Matarrese & Riotto 2005). The latter contributions to non-Gaussianity are usually expressed through a *non-linearity parameter*  $f_{\text{NL}}$  which measures the strength of quadratic terms in the *primordial* gravitational potential (e.g. Salopek & Bond 1990, 1991; Gangui et al. 1994; Verde et al. 2000a). The most stringent limits on  $f_{\text{NL}}$  are based on the analysis of CMB anisotropies from three-year WMAP data (Spergel et al. 2006) and give  $-54 < f_{\text{NL}} < 114$  ( $3\sigma$  confidence level). The high-resolution observations of CMB anisotropies by the *Planck* satellite should reduce the  $3\sigma$  detection threshold to  $|f_{\text{NL}}| \sim 10$ . Searches for primordial NG based on the large-scale structure of the Universe where the relevant observables probe the dark matter density field (e.g. three-point statistics of the galaxy distribution) are plagued with two problems. First, the density field is related to the gravitational potential through the Poisson equation so that its Fourier modes weigh the NG contributions with extra  $k^{-2}$  terms and only the largest scales may keep memory of primordial NG. Moreover, the ratio of Newtonian non-linear terms to intrinsic NG terms roughly scales like  $(1+z)^{-1}$ , so that NG signatures in the local Universe are easily masked by the effects of gravitational instability. In this sense, the 21-cm background at large redshifts appears as an extremely promising dataset to search for primordial NG able to provide constraints on  $f_{\text{NL}}$  which can be complementary and possibly competitive with those based on CMB anisotropies.

Low-frequency radio observations with high angular resolution are limited by the Earth's ionosphere. This layer

<sup>1</sup> Institute for Astronomy, ETH Zürich, 8093 Zürich, Switzerland

<sup>2</sup> Dipartimento di Fisica "G. Galilei", Università di Padova, and INFN Sezione di Padova, via Marzolo 8, I-35131 Padova, Italy

of the atmosphere is opaque to electromagnetic waves whose frequency lies below the local plasma frequency which corresponds to  $\sim 15$  MHz during day-time and near sunspot maximum and to  $\sim 10$  MHz at night near sunspot minimum. These figures are somewhat lower (down to  $\sim 2$  MHz) at preferred sites located near the magnetic poles but, in general, the propagation properties of radio waves with frequencies  $\nu < 30$  MHz show extreme variations due to ionospheric scintillation (e.g. Kassim et al. 1993). Therefore, it is unlikely that ground-based experiments with high angular resolution ( $< 1$  arcmin) will ever measure the properties of the 21-cm background at a redshift  $z \gg 10$ . Space observatories are needed to overcome these limits.

The layout of the paper is as follows. In §2 we summarize the physics of 21-cm radiation and perform the expansion of its brightness temperature to the second perturbative order in all the relevant quantities. Non-Gaussian density fields are introduced in §3. The calculation of the angular bispectrum of redshifted 21-cm fluctuations is presented in §4. Finally, in §5, we estimate the detectability of non-Gaussian features (both primordial and gravity induced) by future experiments and conclude.

We consider a ‘‘concordance’’ cosmological model with a present-day matter-density parameter  $\Omega_m = 0.27$  (of which  $\Omega_b = 0.049$  in baryons), a cosmological constant contribution of  $\Omega_\Lambda = 0.73$  and a Hubble constant of  $H_0 = 100 h \text{ km s}^{-1} \text{ Mpc}^{-1}$  with  $h = 0.71$ . We also assume a Harrison-Zel’dovich primordial power spectrum with spectral index  $n = 1$  and a cold dark matter (CDM) transfer function with present-day normalization  $\sigma_8 = 0.9$  (where  $\sigma_8$  denotes the linear rms fluctuation within a sphere with a comoving radius of  $8 h^{-1} \text{ Mpc}$ ).

## 2. THE 21-CM FLUCTUATIONS

### 2.1. Kinetic temperature of the IGM

About  $3 \times 10^5$  yr after inflation, atomic nuclei and electrons combined to form neutral atoms, and greatly reduced their coupling with photons. Soon after, when the free-streaming CMB radiation cooled below 3000 K and shifted into the infrared, the Universe became dark. The cosmic dark ages persisted until the first luminous sources formed inside virialized density perturbations ( $z \sim 30$ ), and reionized the opaque IGM. The exact timing of this event is still uncertain, even though observational data bracket it between redshift 20 and 6 (e.g. Loeb & Barkana 2001; Spergel et al. 2006).

The kinetics of recombination and ionization processes in a rapidly expanding Universe leaves a residual degree of ionization even during the dark ages. At  $z \simeq 200$ , the mean hydrogen ionization fraction  $\bar{x} \simeq 10^{-4}$  while the fraction of singly ionized Helium is much lower ( $\simeq 10^{-9}$ ). These figures slightly decrease with time due to the cosmic expansion but always remain of the same order of magnitude (e.g. Seager et al. 2000 and references therein).

Compton scattering of CMB photons off free electrons couples the kinetic temperature of cosmic gas  $T_{\text{gas}}$  with the temperature of the photon background (Weymann 1965)

$$\frac{\partial T_{\text{gas}}}{\partial t} - \frac{2}{3} \frac{T_{\text{gas}}}{n_{\text{tot}}} \frac{\partial n_{\text{tot}}}{\partial t} = \frac{8}{3} \frac{\sigma_T U n_e}{m_e c n_{\text{tot}}} (T_{\text{CMB}} - T_{\text{gas}}), \quad (1)$$

where  $\sigma_T$  is the Thomson scattering cross section,  $m_e$  the electron mass and  $c$  the speed of light in vacuum. The total number density of particles,  $n_{\text{tot}}$ , appears on the right-hand side because collisions and Coulomb scatterings hold all the different species (electrons, ions and atoms) at the same temperature. Here  $U$  represents the radiation energy density  $U = \int_0^\infty u_\nu d\nu$  where  $u_\nu = 4\pi J_\nu/c$  and  $J_\nu = (1/4\pi) \int_{4\pi} I_\nu d\hat{n}$  with  $I_\nu$  the specific intensity of radiation (energy per unit time, surface, frequency and solid angle) and  $d\hat{n}$  the solid-angle element. In thermal equilibrium, the radiation field has a frequency distribution given by the Planck function  $J_\nu = B_\nu(T_{\text{CMB}})$  and the total energy is given by Stefan’s law  $U = (\pi^2 k_B^4/15 \hbar^3 c^3) T_{\text{CMB}}^4$  where  $k_B$  and  $\hbar$  denote the Boltzmann and the Planck constants, respectively. Note that the spectrum of the CMB remains close to a blackbody because the heat capacity of radiation is very much larger than that of matter (i.e. there are vastly more photons than baryons). For a uniform distribution of baryons with physical number density  $n_{\text{tot}} \propto (1+z)^3$ , Compton scattering is efficient down to a redshift  $z \sim 150 (\Omega_b h^2/0.023)^{2/5}$  (the decoupling era, e.g. Peebles 1993) and keeps  $T_{\text{gas}} = T_{\text{CMB}} = 2.73(1+z)$  K. Subsequently, the gas expands adiabatically,  $T_{\text{gas}} \propto (1+z)^2$ .

### 2.2. Spin temperature of neutral hydrogen

Neutral hydrogen interacts with radiation of wavelength  $\lambda_{21} = 21.12$  cm through the resonant transition between the two hyperfine levels of the 1s state. This corresponds to a frequency  $\nu_{21} = 1420.4$  MHz and a temperature  $T_* = 0.068$  K. It is convenient to express the ratio between the number density of hydrogen atoms in the excited state,  $n_*$ , and in the ground state,  $n_o$ , in terms of a Boltzmann factor which defines the spin temperature,  $T_s$ :

$$\frac{n_*}{n_o} = \frac{g_*}{g_o} \exp\left(-\frac{T_*}{T_s}\right), \quad (2)$$

where  $g_* = 3$  and  $g_o = 1$  are the spin-degeneracy factors of the excited and fundamental levels in the 1s state. The total density of neutral hydrogen atoms is  $n_{\text{HI}} = n_o + n_*$ . During the dark ages, the time evolution of  $n_o$  is the result of the combined effect of atomic collisions and radiative interactions with the photon background. Approximating the 21-cm transition as infinitely sharp, one gets

$$\left(\frac{\partial}{\partial t} + 3\frac{\dot{a}}{a}\right) n_o = -n_o (C_{01} + B_{01} 4\pi J_{\nu_{21}}) + n_* (C_{10} + A_{10} + B_{10} 4\pi J_{\nu_{21}}), \quad (3)$$

where  $a(t) = (1+z)^{-1}$  is the cosmic scale factor,  $A_{10} = 2.85 \times 10^{-15} \text{ s}^{-1}$  is the spontaneous decay rate of the hyperfine transition of atomic hydrogen,  $C_{01}$  and  $C_{10}$  are the collisional excitation and de-excitation rates, while  $B_{01}$  and  $B_{10}$  are the Einstein rate coefficients. At equilibrium, detailed balancing of collisional and radiative processes gives

$$\frac{C_{01}}{C_{10}} = \frac{g_*}{g_o} \exp\left(-\frac{T_*}{T_{\text{gas}}}\right), \quad \frac{A_{10}}{B_{01}} = \frac{g_o}{g_*} 4\pi F_{\nu_{21}}, \quad \frac{B_{10}}{B_{01}} = \frac{g_o}{g_*}, \quad (4)$$

with  $F_\nu = 4\pi \hbar \nu^3 / c^2$ . When  $T_{\text{gas}}, T_{\text{CMB}}$  and  $T_s$  are much larger than  $T_*$ , all the Boltzmann and the Bose-Einstein factors can be linearized, so as to obtain:

$$\frac{1}{1 + (g_*/g_o)} \frac{d}{dt} \left(\frac{T_*}{T_s}\right) = C_{10} \left(\frac{T_*}{T_{\text{gas}}} - \frac{T_*}{T_s}\right) + A_{10} \left(1 - \frac{T_{\text{CMB}}}{T_s}\right), \quad (5)$$

where the collisional de-excitation rate,  $C_{10} = (4/3) \kappa_{10} n_{\text{HI}}$ , with  $\kappa_{10}$  a function of  $T_{\text{gas}}$  tabulated by Zygelman (2005). At mean density, the characteristic timescales for reaching an equilibrium state are  $T_*/(A_{10} T_{\text{CMB}}) \simeq 5.4 \times 10^3 [(1+z)/51]^{-1} \text{ yr}$  for radiative processes and  $C_{10}^{-1} \simeq 1.2 \times 10^4 (1+\delta)^{-1} [(1+z)/51]^{-5} \text{ yr}$  for atomic collisions (assuming that  $\kappa_{10} \propto T_{\text{gas}}$  which is accurate for  $z \sim 50$  where  $T_{\text{gas}} \sim 50 \text{ K}$ ). Since these timescales are much shorter than the Hubble time, for cosmological studies one is only interested in the steady state solution of equation (5)

$$T_s = \frac{T_{\text{CMB}} + Y_c T_{\text{gas}}}{1 + Y_c}, \quad \text{with} \quad Y_c = \frac{C_{10} T_*}{A_{10} T_{\text{gas}}}. \quad (6)$$

In other words, atomic collisions drive  $T_s$  towards  $T_{\text{gas}}$  while 21-cm transitions drive it towards  $T_{\text{CMB}}$ . Which process dominates depends on the local gas density and collisions become less and less effective with time. For regions at mean density,  $T_s$  departs from  $T_{\text{gas}}$  at  $z \sim 100$  and approaches  $T_{\text{CMB}}$  at  $z \sim 30$ . On the other hand, at  $z \sim 50$  collisions are efficient only within regions with overdensities such that  $1 + \delta > 2.2 [(1+z)/51]^{-4}$ .

This picture is modified by the appearance of the first luminous objects at  $z \lesssim 30$ . At this epoch, bubbles of ionized material start appearing around the sources of light while neutral gas is heated by collisions with fast electrons produced by penetrating photons (X-rays and UV radiation). The detailed evolution of both these phenomena depends on uncertain astrophysical details about the formation of massive stars, X-ray binaries and accreting black holes. Anyway, the presence of Ly $\alpha$  photons provides an additional coupling between  $T_s$  and  $T_{\text{gas}}$  through the so called Wouthuysen-Field effect (Wouthuysen 1952; Field 1958). According to this mechanism, the populations of the singlet and triplet 1s states can be mixed up by the absorption of Ly $\alpha$  photons followed by a radiative decay. The efficiency of the effect is determined by the frequency dependence and the intensity of the background radiation field  $J_\nu$  near Ly $\alpha$ . This is conveniently expressed in terms of the coupling coefficient  $Y_\alpha$  (the Ly $\alpha$  pumping efficiency) and the color temperature  $T_\alpha$  defined as

$$Y_\alpha = \frac{P_{10} T_*}{A_{10} T_\alpha}, \quad \frac{1}{k_B T_\alpha} = -\frac{\partial \log N_\nu}{\partial h\nu} \quad (7)$$

where  $N_\nu = J_\nu / F_\nu$  gives the photon occupation number at frequency  $\nu$  and  $P_{10} = (4/27) P_\alpha$  is the indirect de-excitation rate of the triplet via absorption of a Ly $\alpha$  photon to the  $n = 2$  level with  $P_\alpha = 4\pi \int \sigma_\nu (J_\nu / 2\pi \hbar \nu) d\nu$  the total Ly $\alpha$  scattering rate and  $\sigma_\nu$  the cross section for Ly $\alpha$  scattering (Madau et al. 1997). In steady state, the spin temperature of neutral hydrogen is a weighted average of  $T_{\text{gas}}, T_{\text{CMB}}$  and  $T_\alpha$

$$T_s = \frac{T_{\text{CMB}} + Y_c T_{\text{gas}} + Y_\alpha T_\alpha}{1 + Y_c + Y_\alpha}. \quad (8)$$

There exists then a critical value of  $P_\alpha = 27 A_{10} T_{\text{CMB}} / 4 T_* \simeq 8.5 \times 10^{-12} [(1+z)/11] \text{ s}^{-1}$  above which  $T_s \simeq T_\alpha$ . This roughly corresponds to  $\sim 1$  Ly $\alpha$  photon per baryon. Note that, in general, background photons emitted as continuum, non-ionizing UV radiation and redshifted into the Ly $\alpha$  resonance represent the dominant source of coupling for  $T_s$  with respect to line photons locally emitted via recombinations and collisional excitations (Madau et al. 1997). Moreover, due to the large cross section for resonant scattering and the recoil of the atoms during photon emission, thermalization of the radiation is very efficient and in virtually all the physically relevant situations  $T_\alpha = T_{\text{gas}}$  (Field 1959b).

### 2.3. Brightness temperature of 21-cm fluctuations

The brightness temperature  $T_b$  of a radiation field is defined as  $I_\nu = B_\nu(T_b)$  and, in the Rayleigh-Jeans limit ( $h\nu/k_B T_b \ll 1$ ),  $T_b = c^2 I_\nu / 2\nu^2 k_B$ . In the absence of energy exchanges between matter and radiation after decoupling, the brightness temperature of the CMB would be  $T_b = T_{\text{CMB}}$ . However, interactions between CMB photons and atoms of neutral hydrogen along the line of sight modify the brightness temperature of the CMB at radio wavelengths. The optical depth for the hyperfine transition at  $\lambda = \lambda_{21} (1+z)$  (once again approximated as infinitely sharp) is (Field 1959a)

$$\tau_{21} = \frac{3 c^3 \hbar A_{10} n_{\text{HI}}}{16 k_B \nu_{21}^2 T_s (\partial v_r / \partial r_{\text{phys}})} \quad (9)$$

where the number density of neutral hydrogen, the spin temperature and the radial velocity gradient (in physical units) are both evaluated at a comoving distance  $r(z)$  along the line of sight. This is obtained in the Sobolev approximation

to account for line photons redshifted in or out of the interaction frequency range by the combined action of Hubble expansion and peculiar velocities (e.g. Sobolev 1960) In the Rayleigh-Jeans limit, the radiative transfer equation for the rest-frame brightness temperature of a patch of the sky at redshift  $z$  gives

$$T_b = T_{\text{CMB}} e^{-\tau_{21}} + T_s (1 - e^{-\tau_{21}}). \quad (10)$$

The effect of the 21-cm spin-flip transition can then be measured as an excess or a decrement of the brightness temperature of the sky (as observed at the present time) at a wavelength  $\lambda = \lambda_{21} (1 + z)$  (Scott & Rees 1990):

$$T_{21} = \frac{T_b - T_{\text{CMB}}}{1 + z} \simeq \frac{T_s - T_{\text{CMB}}}{1 + z} \tau_{21}. \quad (11)$$

The last equality holds in the optically thin limit which always applies since, neglecting peculiar velocities,

$$\tau_{21} \simeq 0.025 \frac{T_{\text{CMB}}}{T_s} \left( \frac{\Omega_b h}{0.035} \right) \left( \frac{\Omega_m}{0.27} \right)^{-1/2} \left( \frac{1+z}{51} \right)^{1/2} \ll 1. \quad (12)$$

The spatial dependence of  $T_{21}$ ,  $T_s$ ,  $T_{\text{CMB}}$  and  $\tau_{21}$  is understood in equation (11) but all these quantities should be evaluated at a comoving distance  $r(z)$  along the line of sight. Note that intrinsic fluctuations of  $T_{\text{CMB}}$  can be fully neglected in this context since they are of the order of a few  $\mu\text{K}$  while those of  $T_{21}$  are roughly a thousand times larger. Given the thermal history of the gas, four regimes can be distinguished: *i*) the pre-decoupling era ( $z \gtrsim 200$ ) when  $T_s = T_{\text{CMB}}$  and no fluctuations are present in the brightness temperature of the 21-cm background; *ii*) the dark ages ( $30 \lesssim z \lesssim 200$ ) when  $T_s \ll T_{\text{CMB}}$  and neutral hydrogen absorbs CMB photons; *iii*) the reionization epoch ( $10 \lesssim z \lesssim 30$ ) when  $T_s \gg T_{\text{CMB}}$  and neutral hydrogen emits CMB photons; *iv*) the post-reionization era ( $z \lesssim 10$ ) when the IGM is nearly fully ionized over most of its volume and  $T_{21} = 0$  almost everywhere (with the exception of the highest density regions).

#### 2.4. Fluctuations of the brightness temperature

The brightness temperature of the CMB at  $\lambda = \lambda_{21} (1 + z)$  cm fluctuates with the position on the sky and redshift reflecting the variation of a number of underlying quantities. An excess in the density of neutral hydrogen (either determined by an overdensity  $\delta$  or by a fluctuation of the ionized fraction  $\delta_x$ ),

$$n_{\text{HI}} = \bar{n}_{\text{H}} [1 - \bar{x} (1 + \delta_x)] (1 + \delta), \quad (13)$$

produces an increment of the optical depth and alters  $T_s$  (directly, by increasing the collision rate, and indirectly, by changing the gas temperature). Radial peculiar velocities,  $v_{\text{pec}}$ , also modify  $\tau_{21}$  through the term

$$\left( \frac{\partial v_r}{\partial r_{\text{phys}}} \right) = H(z) + (1 + z) \frac{\partial v_{\text{pec}}}{\partial r}, \quad (14)$$

where  $H(z)$  is the Hubble parameter at redshift  $z$ . Finally, during reionization, also fluctuations in the intensity and temperature of the Ly $\alpha$  background become important.

For small fluctuations, we perform a perturbative expansion of the interesting quantities by writing  $\delta_i = \sum_n \delta_i^{(n)}/n!$  where  $\delta_i^{(n)} = \mathcal{O}[(\delta_i^{(1)})^n]$  and the subscript  $i$  indicates a particular random field (e.g. temperature, density, etc.). In order to compute the first non-vanishing term of the bispectrum we need to expand  $T_{21}$  up to 2<sup>nd</sup> order in  $\delta$ ,  $\delta_x$ ,  $v_{\text{pec}}$ , and  $\delta_\alpha$  (i.e. the fluctuation in the pumping efficiency of the Ly $\alpha$  background,  $Y_\alpha$ ). Fluctuations of  $T_{\text{gas}} = \bar{T}_{\text{gas}} (1 + \delta_T)$  can be expressed in terms of the density perturbations through the following functional expansion in real space:

$$\delta_T(\mathbf{r}, z) = \int d^3 \mathbf{x}_1 \mathcal{G}_1(\mathbf{x}_1, z) \delta(\mathbf{r} + \mathbf{x}_1, z) + \int d^3 \mathbf{x}_1 \int d^3 \mathbf{x}_2 \mathcal{G}_2(\mathbf{x}_1, \mathbf{x}_2, z) \delta(\mathbf{r} + \mathbf{x}_1, z) \delta(\mathbf{r} + \mathbf{x}_2, z) + \dots \quad (15)$$

where the dots denote  $n$ -point non-local dependencies with  $n > 2$ . Both kernels  $\mathcal{G}_1$  and  $\mathcal{G}_2$  vanish before decoupling when Compton scattering keeps  $T_{\text{gas}} = T_{\text{CMB}}$ . On the other hand, at late times, when the gas expands adiabatically, all the terms in equation (15) are local:  $\mathcal{G}_1(\mathbf{x}, z) = (2/3) \delta_{\text{D}}(\mathbf{x})$  and  $\mathcal{G}_2(\mathbf{x}_1, \mathbf{x}_2, z) = -(2/9) \delta_{\text{D}}(\mathbf{x}_1) \delta_{\text{D}}(\mathbf{x}_2)$  where  $\delta_{\text{D}}(\mathbf{x})$  is the Dirac delta function. The complete redshift evolution between these asymptotic regimes is determined by equation (1), that can be rewritten as

$$\frac{\partial \delta_T}{\partial t} - \frac{2}{3} \frac{1 + \delta_T}{1 + \delta} \frac{\partial \delta}{\partial t} = -C(t) \delta_T; \quad (16)$$

where,  $C(t) = (8 \sigma_T U n_e T_{\text{CMB}})/(3 m_e c n_{\text{tot}} \bar{T}_{\text{gas}})$ . Solutions for the kernels  $\mathcal{G}_1$  and  $\mathcal{G}_2$  are derived in Appendix A where it is shown that  $\mathcal{G}_1(\mathbf{x}, z) = g_1(z) \delta_{\text{D}}(\mathbf{x})$  at all epochs while  $\mathcal{G}_2$  has a complex spatial dependence. These results extend the linear analysis by Bharadwaj & Ali (2004) to second order (our function  $g_1$  corresponds to their linear parameter  $g$ ). Note that these authors use a similar technique to relate fluctuations in  $T_s$  and  $\delta$  through equation (5). Here, instead, we perturb the steady state solution given in equation (8) which allows us to explicit the dependence on the underlying variables in analytic form.

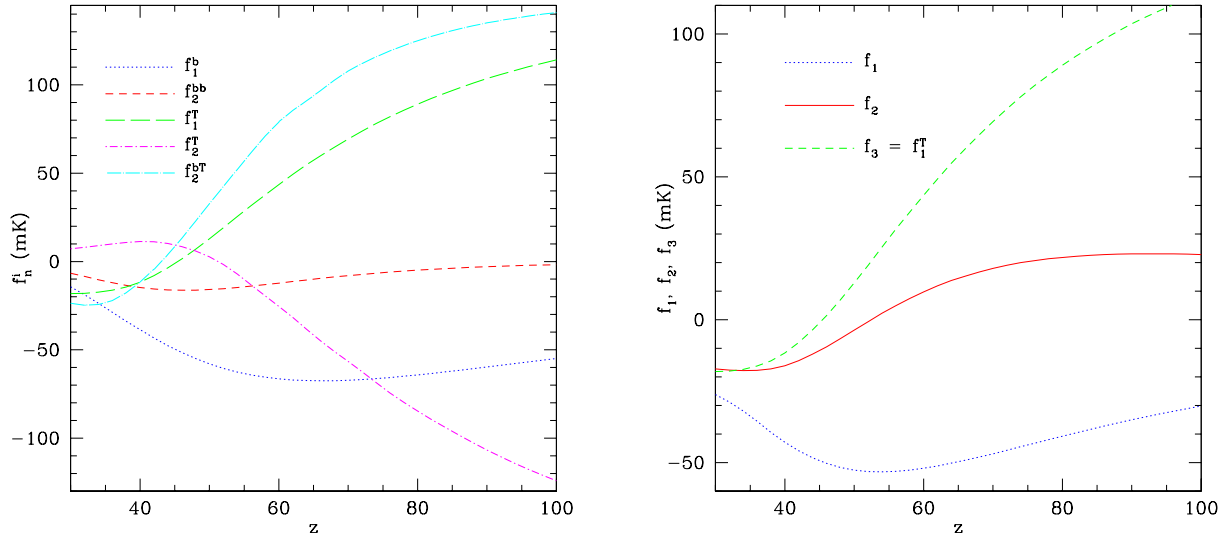


FIG. 1.— Left: Redshift evolution of the coefficients that couple the brightness-temperature fluctuations to perturbations in the gas temperature and density (see the main text and both the Appendices for details). Right: Evolution of the “effective” coupling coefficients  $f_1$ ,  $f_2$  and  $f_3 = f_1^T$  introduced in equation (17).

The most general expansion of  $T_{21}$  in terms of all the possible sources of spatial fluctuations up to second order is reported in Appendix B. Here, we focus on the 21-cm signal coming from the dark ages. We therefore neglect fluctuations in the Ly $\alpha$  background and we consider inhomogeneities in the hydrogen ionization fraction whose contribution is depressed by a factor of  $\sim \bar{x}/(1-\bar{x}) \simeq 10^{-4}$  with respect to that generated by density fluctuations. As a first step, we also ignore peculiar velocities, postponing to future work a detailed study of their subdominant effects. In this case, the spatial fluctuations of the brightness temperature can be written as

$$\begin{aligned} \Delta T_{21}(\mathbf{r}, z) &= T_{21}(\mathbf{r}, z) - T_{21}^{(0)}(z) \\ &= f_1(z) \left( \delta^{(1)}(\mathbf{r}, z) + \frac{1}{2} \delta^{(2)}(\mathbf{r}, z) \right) + f_2(z) \delta^{(1)}(\mathbf{r}, z)^2 + \\ &\quad + f_3(z) \int d^3 \mathbf{x}_1 \int d^3 \mathbf{x}_2 \mathcal{G}_2(\mathbf{x}_1, \mathbf{x}_2, z) \delta(\mathbf{r} + \mathbf{x}_1, z) \delta(\mathbf{r} + \mathbf{x}_2, z), \end{aligned} \quad (17)$$

where

$$T_{21}^{(0)} = f_0 \left( 1 - \frac{T_{\text{CMB}}}{S} \right) (1 - \bar{x}) \quad (18)$$

and, since  $H(z) \simeq H_0 \Omega_m^{1/2} (1+z)^{3/2}$  for  $z \gg 1$ ,

$$f_0 = \left( \frac{3c^3 \hbar A_{10}}{16k_B \nu_{21}} \right) \frac{\bar{n}_{\text{HI}}}{H_0} \left( \frac{1+z}{\Omega_{m,o}} \right)^{1/2} \simeq 69.05 \text{ mK} \left( \frac{\Omega_b h}{0.035} \right) \left( \frac{\Omega_m}{0.27} \right)^{-1/2} \left( \frac{1+z}{51} \right)^{1/2}. \quad (19)$$

The functions  $f_1$ ,  $f_2$  and  $f_3$  are different combinations of the coefficients that couple the brightness temperature with the local baryonic density (superscript b) and the gas temperature (superscript T):

$$f_1 = f_1^b + g_1 f_1^T; \quad (20)$$

$$f_2 = f_2^{bb} + g_1^2 f_2^{TT} + g_1 f_2^{bT}; \quad (21)$$

$$f_3 = f_1^T. \quad (22)$$

Analytic expressions for these coupling constants are given in Appendix B and their behaviour as a function of redshift is shown in Figure 1. An overdensity of order unity gives rise to a fluctuation in  $T_{21}$  of a few tens of mK and the expected signal is maximum at  $z \simeq 50$ . Note that  $f_2$  and  $f_3$  change sign with redshift and multifrequency experiments can be used to isolate the contributions of the different terms in equation (17).

### 3. NON-GAUSSIAN DENSITY FIELDS

#### 3.1. The bispectrum

From now on it will be convenient to work in Fourier space. We define the Fourier transform of the random field  $X(\mathbf{r})$  as  $\tilde{X}(\mathbf{k}) = \int d^3 \mathbf{r} X(\mathbf{r}) \exp(-i\mathbf{k} \cdot \mathbf{r})$ , where  $\mathbf{r} = r\hat{\mathbf{n}}$ . For a stationary random field (statistically invariant under

rotations and translations), the power spectrum  $P(k)$  is given by the ensemble average

$$\langle \delta \tilde{X}(\mathbf{k}_1) \delta \tilde{X}(\mathbf{k}_2) \rangle = (2\pi)^3 P(k_1) \delta_{\text{D}}(\mathbf{k}_1 + \mathbf{k}_2). \quad (23)$$

Similarly, the bispectrum  $B(\mathbf{k}_1, \mathbf{k}_2, \mathbf{k}_3)$  is defined as

$$\langle \delta \tilde{X}(\mathbf{k}_1) \delta \tilde{X}(\mathbf{k}_2) \delta \tilde{X}(\mathbf{k}_3) \rangle = (2\pi)^3 B(\mathbf{k}_1, \mathbf{k}_2, \mathbf{k}_3) \delta_{\text{D}}(\mathbf{k}_1 + \mathbf{k}_2 + \mathbf{k}_3). \quad (24)$$

For a Gaussian random field,  $B = 0$ .

### 3.2. Non-Gaussianity from gravitational instability

For the range of scales and redshifts considered here, the baryons trace the dark matter, so that we can speak of a unique overdensity  $\delta = \delta^{(1)} + \frac{1}{2}\delta^{(2)} + \mathcal{O}(\delta^{(3)})$ , where the Fourier-space expressions for the first and second-order terms read, respectively

$$\tilde{\delta}^{(1)}(\mathbf{k}, z) = D_+(z) \tilde{\delta}_0^{(1)}(\mathbf{k}) \quad (25)$$

and

$$\frac{1}{2} \tilde{\delta}^{(2)}(\mathbf{k}, z) = \frac{D_+^2(z)}{(2\pi)^3} \int d^3 \mathbf{q}_1 \int d^3 \mathbf{q}_2 \delta_{\text{D}}(\mathbf{q}_1 + \mathbf{q}_2 - \mathbf{k}) \mathcal{K}(\mathbf{q}_1, \mathbf{q}_2, z) \tilde{\delta}_0^{(1)}(\mathbf{q}_1) \tilde{\delta}_0^{(1)}(\mathbf{q}_2), \quad (26)$$

where  $D_+(z)$  is the linear grow factor of density fluctuations and  $\delta_0^{(1)}$  is the matter overdensity linearly extrapolated till the present epoch (i.e. at  $z = 0$  when  $D_+ = 1$ ). For the density field originated via gravitational instability of Gaussian initial conditions, the kernel  $\mathcal{K}$  assumes the form (e.g. Fry 1984)

$$\mathcal{K}_{\text{L}}(\mathbf{k}_1, \mathbf{k}_2) = \frac{5}{7} + \frac{2}{7} \cos^2 \theta_{12} + \frac{1}{2} \left( \frac{k_1}{k_2} + \frac{k_2}{k_1} \right) \cos \theta_{12} \quad (27)$$

with  $\cos \theta_{12} = \hat{\mathbf{k}}_1 \cdot \hat{\mathbf{k}}_2$  and  $\hat{\mathbf{k}} = \mathbf{k}/k$ . This holds at high-redshift (where the mass density parameter approaches unity).

### 3.3. Primordial non-Gaussianity

For a large class of models for the generation of the initial seeds for structure formation, including standard single-field and multi-field inflation, the curvaton and the inhomogeneous reheating scenarios, the level of primordial non-Gaussianity can be modeled through a quadratic term in Bardeen's gauge-invariant potential  $\Phi$ ,<sup>3</sup> namely

$$\Phi = \Phi_{\text{L}} + f_{\text{NL}} (\Phi_{\text{L}}^2 - \langle \Phi_{\text{L}}^2 \rangle), \quad (28)$$

where  $\Phi_{\text{L}}$  is a Gaussian random field and the specific value of the dimensionless non-linearity parameter  $f_{\text{NL}}$  depends on the assumed scenario (e.g. Bartolo et al. 2004). The kernel

$$\mathcal{K}(\mathbf{q}_1, \mathbf{q}_2, z) = \mathcal{K}_{\text{L}}(\mathbf{q}_1, \mathbf{q}_2) + \mathcal{K}_{\text{NL}}(\mathbf{q}_1, \mathbf{q}_2, z) \quad (29)$$

with

$$\mathcal{K}_{\text{NL}}(\mathbf{q}_1, \mathbf{q}_2, z) = 6 f_{\text{NL}} E(z) \frac{T(|\mathbf{q}_1 + \mathbf{q}_2|)}{T(q_1) T(q_2)} \left( \frac{1}{q_1^2} + \frac{1}{q_2^2} + \frac{2}{q_1 q_2} \cos \theta_{12} \right) \quad (30)$$

accounts for both the non-linear effects of gravitational instability ( $\mathcal{K}_{\text{L}}$ ) and the evolved non-Gaussian contribution ( $\mathcal{K}_{\text{NL}}$ ). Here  $E(z) = H_0^2 \Omega_{0m} / (4c^2 D_+(z))$ , and  $T(k)$  is the linear transfer function for CDM.

It is worth stressing that equation (28), even though commonly used, is not generally valid: detailed second-order calculations of the evolution of perturbations from the inflationary period to the present time show that the quadratic, non-Gaussian contribution to the gravitational potential should be represented as a convolution with a kernel  $f_{\text{NL}}(\mathbf{x}, \mathbf{y})$  rather than a product (in full analogy with the quadratic term in equation (15)). Indeed, for scales which entered the Hubble radius during matter dominance, the calculation of  $f_{\text{NL}}$  can be performed analytically in the so-called Poisson gauge (Bartolo, Matarrese & Riotto 2005) and leads to the Fourier space expression:

$$\begin{aligned} \tilde{f}_{\text{NL}}(\mathbf{k}_1, \mathbf{k}_2; z) = & \frac{5}{3} (a_{\text{nl}} - 1) + \frac{77(\mathbf{k}_1 \cdot \mathbf{k}_2) - 102(k_1^2 + k_2^2)}{42k^2} + \\ & - \frac{(k_1^2 + k_2^2)(\mathbf{k}_1 \cdot \mathbf{k}_2)}{k_1^2 k_2^2 k^2} \left( \frac{4}{7} (\mathbf{k}_1 \cdot \mathbf{k}_2) + k_1^2 + k_2^2 \right) \\ & + \frac{6 k_1^2 k_2^2}{7 k^4} - \frac{6 (\mathbf{k}_1 \cdot \mathbf{k}_2)^2}{7 k^4} + \mathcal{O}(E(z)^2/k^4), \end{aligned} \quad (31)$$

where the parameter  $a_{\text{nl}} - 1$  quantifies the amount of non-Gaussianity produced during (or immediately after) inflation. For the simplest case of single-field slow-roll inflation,  $|a_{\text{nl}} - 1| \ll 1$ , being of the order of the slow-roll parameters

<sup>3</sup> On scales much smaller than the Hubble radius, Bardeen's gauge-invariant potential would reduce to minus the usual peculiar gravitational potential.

(Gangui et al. 1994; Acquaviva et al. 2003; Maldacena 2003), while alternative models, like the curvaton or the inhomogeneous reheating scenarios, may easily accomodate much larger values of  $a_{\text{nl}} - 1$  (see Bartolo et al. 2004 and references therein), such that all momentum-dependent contributions to  $\tilde{f}_{\text{NL}}$  can be neglected and the non-linearity parameter can be effectively approximated with a constant,  $\tilde{f}_{\text{NL}} \approx \frac{5}{3}(a_{\text{nl}} - 1)$ , as assumed in the present analysis (see equation (28)).

From the expressions above, one can easily obtain the (tree-level) bispectrum of density perturbations evaluated at three different redshifts as

$$B(\mathbf{k}_1, \mathbf{k}_2, \mathbf{k}_3, z_1, z_2, z_3) = 2 \mathcal{K}(\mathbf{k}_1, \mathbf{k}_2, z_1) D_+(z_1)^2 D_+(z_2) D_+(z_3) P_0(k_1) P_0(k_2) + \text{cycl.}, \quad (32)$$

where  $P_0(k)$  is the linear power-spectrum of density fluctuation extrapolated till the present epoch. The above expressions tell us that the optimal strategy to constrain non-Gaussianity in the large-scale structure of the Universe is to use large-scale and/or high-redshifts datasets (e.g. Verde, Heavens & Matarrese 2000b; Verde et al. 2001; Scoccimarro, Sefusatti & Zaldarriaga 2004). From this point of view, the 21-cm fluctuations potentially represent a very powerful tool to detect non-Gaussianity which could complement the limits obtained from the study of CMB anisotropies (e.g. Spergel et al. 2006).

## 4. THE ANGULAR BISPECTRUM OF 21-CM FLUCTUATIONS

### 4.1. Definition

The observed brightness temperature is a convolution of  $T_{21}$  with a frequency-dependent instrumental response  $W_\nu(r)$  (from now on the window function):

$$T_{21}^{\text{obs}}(\hat{\mathbf{n}}) = \int dr W_\nu(r) T_b(r\hat{\mathbf{n}}). \quad (33)$$

The window function peaks at the central frequency of the detector,  $\nu$ , and is different from zero within a characteristic frequency range corresponding to the bandwidth of the instrument. For analytic convenience we prefer here to express  $W_\nu$  in terms of the comoving distance  $r$  evaluated at  $z = \nu_{21}/\nu - 1$ .

The fluctuations of the observed <sup>4</sup> brightness temperature can be expanded in spherical harmonics:

$$\Delta T_{21}(\hat{\mathbf{n}}) = \sum_{\ell=0}^{\infty} \sum_{m=-\ell}^{\ell} a_{\ell m} Y_{\ell m}(\hat{\mathbf{n}}), \quad a_{\ell m} = \int d^2\hat{\mathbf{n}} \Delta T_{21}(\hat{\mathbf{n}}) Y_{\ell m}^*(\hat{\mathbf{n}}). \quad (34)$$

The angular bispectrum is then given by the ensemble average

$$B_{\ell_1 \ell_2 \ell_3}^{m_1 m_2 m_3} = \langle a_{\ell_1 m_1} a_{\ell_2 m_2} a_{\ell_3 m_3} \rangle, \quad (35)$$

which for an isotropic random field can be re-written in terms of the angle-averaged bispectrum  $B_{\ell_1 \ell_2 \ell_3}$  as

$$B_{\ell_1 \ell_2 \ell_3}^{m_1 m_2 m_3} = \begin{pmatrix} \ell_1 & \ell_2 & \ell_3 \\ m_1 & m_2 & m_3 \end{pmatrix} B_{\ell_1 \ell_2 \ell_3}. \quad (36)$$

Here the matrix denotes the Wigner-3j symbol so that  $B_{\ell_1 \ell_2 \ell_3}^{m_1 m_2 m_3}$  does not vanish only when:

1.  $|\ell_j - \ell_k| \leq \ell_i \leq \ell_j + \ell_k$  for all permutations of indices  $i, j, k$ ;
2.  $\ell_1 + \ell_2 + \ell_3 = \text{even}$ ;
3.  $m_1 + m_2 + m_3 = 0$ .

### 4.2. Derivation

The angular bispectrum of the 21-cm background is then <sup>5</sup>

$$\langle a_{\ell_1 m_1} a_{\ell_2 m_2} a_{\ell_3 m_3} \rangle = \int d\hat{\mathbf{n}}_1 d\hat{\mathbf{n}}_2 d\hat{\mathbf{n}}_3 \int dr_1 dr_2 dr_3 W_\nu(r_1) W_\nu(r_2) W_\nu(r_3) \langle \Delta T_{21}(\mathbf{r}_1) \Delta T_{21}(\mathbf{r}_2) \Delta T_{21}(\mathbf{r}_3) \rangle Y_{\ell_1 m_1}^*(\hat{\mathbf{n}}_1) Y_{\ell_2 m_2}^*(\hat{\mathbf{n}}_2) Y_{\ell_3 m_3}^*(\hat{\mathbf{n}}_3), \quad (37)$$

where the three-point correlation function is

$$\langle \Delta T_{21}(\mathbf{r}_1) \Delta T_{21}(\mathbf{r}_2) \Delta T_{21}(\mathbf{r}_3) \rangle = \int \frac{d^3\mathbf{k}_1 d^3\mathbf{k}_2 d^3\mathbf{k}_3}{(2\pi)^6} B_{21}(\mathbf{k}_1, \mathbf{k}_2, \mathbf{k}_3, z_1, z_2, z_3) \delta_{\text{D}}(\mathbf{k}_1 + \mathbf{k}_2 + \mathbf{k}_3) e^{i(\mathbf{k}_1 \mathbf{r}_1 + \mathbf{k}_2 \mathbf{r}_2 + \mathbf{k}_3 \mathbf{r}_3)} \quad (38)$$

with  $B_{21}(\mathbf{k}_1, \mathbf{k}_2, \mathbf{k}_3, z_1, z_2, z_3)$  the three-dimensional bispectrum of  $\Delta T_{21}$ .

<sup>4</sup> In order to simplify the notation, from now on we drop the superscript ‘‘obs’’ to indicate the observed brightness temperature.

<sup>5</sup> We just consider the case of a single window function. The generalization of our results to multi-frequency analyses is straightforward.

4.2.1. *Bispectrum from gravitational instability*

We first account for the non-Gaussianity generated by gravitational instability from Gaussian initial conditions. In this case, the integral over  $\mathbf{k}_3$  in equation (38) can be easily computed exploiting the Dirac delta function. We then expand the exponential term in the same equation into spherical harmonics and perform all the angular integrations. On scales where the baryon distribution traces the density fluctuations of the dark matter,

$$B_{21}(\mathbf{k}_1, \mathbf{k}_2, \mathbf{k}_3, z_1, z_2, z_3) = 2 \mathcal{K}_{21}(\mathbf{k}_1, \mathbf{k}_2, z_1) D_+(z_1)^2 D_+(z_2) D_+(z_3) f_1(z_1) f_1(z_2) f_1(z_3) P_0(k_1) P_0(k_2) + \text{cycl.} \quad (39)$$

where the kernel  $\mathcal{K}_{21}$  can be written as a power series of  $\cos \theta_{12}$ ,

$$2 \mathcal{K}_{21}(\mathbf{k}_1, \mathbf{k}_2, z) = A_0 + A_1 \cos \theta_{12} + A_2 \cos^2 \theta_{12} \quad (40)$$

with

$$A_0 = \frac{10}{7} + \frac{f_3}{f_1} g_{2a} + \frac{f_2}{f_1}, \quad A_1 = \left(1 + \frac{f_3}{f_1} g_{2c}\right) \left(\frac{k_1}{k_2} + \frac{k_2}{k_1}\right), \quad A_2 = \frac{4}{7} + \frac{f_3}{f_1} g_{2b}. \quad (41)$$

The factors  $g_{2a}, g_{2b}, g_{2c}$  are functions of time that parameterize the evolution of the kernel  $\mathcal{G}_2$  and thus take into account gas temperature perturbations up to second order in  $\delta$  as indicated in Appendix A. After long but straightforward calculations (see Verde et al. 2000b for a similar case), the expression for the angular bispectrum of the 21-cm background can be written as a sum of cyclic terms

$$B_{\ell_1 \ell_2 \ell_3} = B_{\ell_1 \ell_2} + B_{\ell_1 \ell_3} + B_{\ell_2 \ell_3} \quad (42)$$

with

$$\begin{aligned} B_{\ell_1 \ell_2} &= \frac{16}{\pi} i^{(\ell_1 + \ell_2)} \sqrt{\frac{(2\ell_1 + 1)(2\ell_2 + 1)(2\ell_3 + 1)}{(4\pi)^3}} \int dk_1 \int dk_2 k_1^2 k_2^2 \\ &\alpha_{\ell_1}(k_1) \alpha_{\ell_2}(k_2) z P_0(k_1) P_0(k_2) \sum_{\ell, \ell_6, \ell_7} i^{(\ell_6 + \ell_7)} (-1)^\ell (2\ell_6 + 1)(2\ell_7 + 1) \\ &\left( \begin{matrix} \ell_1 & \ell_6 & \ell \\ 0 & 0 & 0 \end{matrix} \right) \left( \begin{matrix} \ell_2 & \ell_7 & \ell \\ 0 & 0 & 0 \end{matrix} \right) \left( \begin{matrix} \ell_3 & \ell_6 & \ell_7 \\ 0 & 0 & 0 \end{matrix} \right) \left\{ \begin{matrix} \ell_1 & \ell_2 & \ell_3 \\ \ell_7 & \ell_6 & \ell \end{matrix} \right\} \\ &\int dr D_+(r)^2 f_1(r) W_\nu(r) j_{\ell_6}(k_1 r) j_{\ell_7}(k_2 r) B_\ell(k_1, k_2, r), \end{aligned} \quad (43)$$

where  $\left\{ \dots \right\}$  indicates a Wigner-6j symbol. Here  $\alpha_\ell(k) = \int dr j_\ell(kr) D_+(r) f_1(r) W_\nu(r)$ , with  $j_\ell(x)$  the spherical Bessel function of the first kind. Note that only terms with  $\ell_6 = \ell_1 - \ell, \dots, \ell_1 + \ell$  and  $\ell_7 = \ell_2 - \ell, \dots, \ell_2 + \ell$  contribute to the sum. The functions  $B_\ell(k_1, k_2, r)$  are generated by the terms in equation (40). Since this power series does not contain exponents larger than 2, only terms with  $\ell = 0, 1, 2$  matter. We thus obtain:

$$B_0 = A_0 + \frac{1}{3} A_2 = \frac{34}{21} + \frac{f_3}{f_1} \left( g_{2a} + \frac{1}{3} g_{2b} \right) + \frac{f_2}{f_1}, \quad (44)$$

$$B_1 = A_1 = \left(1 + \frac{f_3}{f_1} g_{2c}\right) \left(\frac{k_1}{k_2} + \frac{k_2}{k_1}\right), \quad (45)$$

$$B_2 = \frac{2}{3} A_2 = \frac{8}{21} + \frac{2}{3} \frac{f_3}{f_1} g_{2b}. \quad (46)$$

For narrow window functions, the expression in equation (43) can be further simplified. In particular, the linear growth factors, the coupling constants  $f_i$  and the time functions  $g_{2i}$  introduced in Appendix A can be evaluated at the epoch corresponding to the central frequency of the detector.

4.2.2. *Bispectrum from primordial non-Gaussianity*

We follow a different procedure to integrate equations (37) and (38) with the kernel  $\mathcal{K}_{\text{NL}}(\mathbf{q}_1, \mathbf{q}_2, z)$  given in equation (30). In this case, it is convenient to expand the Dirac delta function in spherical harmonics and perform the angular integrations (e.g. Komatsu & Spergel 2001). The result is

$$B_{\ell_1 \ell_2 \ell_3} = \frac{16}{\pi^3} f_{\text{NL}} \sqrt{\frac{(2\ell_1 + 1)(2\ell_2 + 1)(2\ell_3 + 1)}{4\pi}} \left( \begin{matrix} \ell_1 & \ell_2 & \ell_3 \\ 0 & 0 & 0 \end{matrix} \right) \int dr r^2 [\beta_{\ell_1}(r) \beta_{\ell_2}(r) \Gamma_{\ell_3}(r) + \text{cycl.}] \quad (47)$$

where

$$\beta_\ell(r) = \int dk \frac{P_0(k)}{T(k)} \alpha_\ell(k) j_\ell(kr) \quad \text{and} \quad \Gamma_\ell(r) = 6 \int dk k^4 T(k) \epsilon_\ell(k) j_\ell(kr), \quad (48)$$

with  $\epsilon_\ell(k) = \int dr' D_+(r')^2 [E(r') f_1(r') + g_{2d}(r') f_3(r')/6] W_\nu(r') j_\ell(kr')$ . Note that, at  $z \simeq 50$ ,  $6E f_1/g_{2d} f_3 \simeq 20$  and the contribution of the non-local kernel  $\mathcal{G}_2$  to  $\epsilon_\ell$  is rather small (see also Figure 4).

### 4.3. Results

We perform a numerical integration of equations (43) and (47). The resulting angular bispectra are shown in Figure 2 for different sets of the parameters  $\ell_1, \ell_2$  and  $\ell_3$  (bispectrum configurations). From top to bottom, we present equilateral ( $B_{\ell\ell\ell}$ ), quasi-equilateral ( $B_{\ell\ell+1\ell-1}$ ) and “squeezed” ( $B_{\ell\ell 2}$ ) configurations. In all cases, we consider an ideal instrument with unlimited angular resolution and characterized by a Gaussian window function with a frequency ( $1\sigma$ ) bandwidth of 0.1 MHz centred around  $z = 50$ . The left panels compare the different contributions due to non-linear gravity – equation (43) – and to primordial non-Gaussianity – equation (47) – with  $f_{\text{NL}} = 1$ . The total non-Gaussian signal in the various configurations and for different values of  $f_{\text{NL}}$  is shown in the right panels of Figure 2. Note that the signal due to gravitational instability dominates at all angular scales. For  $\ell < 200$ , the ratio between the two contributions is  $\sim 50$ . This difference becomes much more severe at smaller angular scales. This happens because any primordial non-Gaussianity in the gravitational potential is going to be shifted to larger scales when observed in the overdensity field as a direct consequence of the Poisson equation.

## 5. DISCUSSION AND CONCLUSIONS

Using second order perturbation theory, we have computed analytically and evaluated numerically the bispectrum of redshifted 21-cm fluctuations down to a few arcsecond angular scales ( $\ell \simeq 10^5$ ). Is the expected signal detectable by future radio experiments? And can the data be used to test the gravitational instability scenario and quantify primordial non-Gaussianity? Suppose we fit the observed bispectrum  $B_{\ell_1\ell_2\ell_3}^{\text{obs}}$  with a theoretical model by minimizing the objective function

$$\chi^2 = \sum_{\ell_1 \leq \ell_2 \leq \ell_3} \frac{\left( B_{\ell_1\ell_2\ell_3}^{\text{obs}} - \sum_i P_i B_{\ell_1\ell_2\ell_3}^{(i)} \right)^2}{\sigma_{\ell_1\ell_2\ell_3}^2} \quad (49)$$

where  $i$  distinguishes the different contributions of non-linear gravity and primordial non-Gaussianity and  $P_i$  is a normalization constant (i.e., for a given set of cosmological parameters,  $P_1 \equiv (\sigma_8/0.9)^4$  and  $P_2 \equiv f_{\text{NL}} (\sigma_8/0.9)^4$ ). If the amount of non-Gaussianity is small, the cosmic variance of the bispectrum is given by the disconnected part of the six-point function of  $a_{\ell m}$  (Luo 1994). The variance of  $B_{\ell_1\ell_2\ell_3}$  is then calculated as (e.g. Spergel & Goldberg 1999)

$$\sigma_{\ell_1\ell_2\ell_3}^2 = \langle B_{\ell_1\ell_2\ell_3}^2 \rangle - \langle B_{\ell_1\ell_2\ell_3} \rangle^2 \simeq \mathcal{C}_{\ell_1} \mathcal{C}_{\ell_2} \mathcal{C}_{\ell_3} \Delta_{\ell_1\ell_2\ell_3}, \quad (50)$$

where  $\Delta_{\ell_1\ell_2\ell_3}$  is equal to 1, 2 or 6 when all the  $\ell$ -indices are different, two of them are the same or all of them are identical, respectively. Here  $\mathcal{C}_\ell$  denotes the total angular power spectrum of the 21-cm background including the contribution of the detector noise. The corresponding Fisher matrix  $F_{ij}$  is

$$F_{ij} = \sum_{\ell_1 \leq \ell_2 \leq \ell_3} \frac{B_{\ell_1\ell_2\ell_3}^{(i)} B_{\ell_1\ell_2\ell_3}^{(j)}}{\sigma_{\ell_1\ell_2\ell_3}^2}, \quad (51)$$

where  $i = 1$  refers to parameter  $P_1$  and  $i = 2$  refers to parameter  $P_2$ . The signal-to-noise ratio  $(S/N)_i$  for the  $i$ -component is given by

$$\left( \frac{S}{N} \right)_i = \frac{1}{\sqrt{F_{ii}^{-1}}}. \quad (52)$$

An order of magnitude estimation of this quantity as a function of the angular resolution  $\ell$  can be obtained neglecting the covariance of the different components, thus writing  $(S/N)_i \simeq \sqrt{F_{ii}}$ . Since the calculation of  $B_{\ell_1\ell_2\ell_3}$  is expensive at high  $\ell$ , we use the configurations in Figure 2 to estimate the total signal-to-noise ratio. Our results are shown in Figure 3: an experiment with arcmin-scale resolution at  $z = 50$  would clearly detect the bispectrum induced by non-linear gravity with  $(S/N) \sim 100$ . On the other hand, for the signal from primordial non-Gaussianity,  $(S/N) \sim 0.1 f_{\text{NL}}$ . Increasing the angular resolution by a factor of 10 would give  $(S/N) \sim 0.3 f_{\text{NL}}$ . We consider here an ideal, full-sky experiment where the measurements are only limited by cosmic variance (i.e. with no detector noise) and where foreground signals can be perfectly subtracted. If only a fraction  $f_{\text{sky}}$  is surveyed, our signal-to-noise estimates should be depressed by a factor  $f_{\text{sky}}^{1/2}$ .

A tomography of the neutral hydrogen distribution within the redshift range  $30 < z < 100$  in slices of bandwidth  $\sim 0.1$  MHz ( $1\sigma$ ) would provide nearly 150 21-cm maps. Since the correlations between different redshift slices will be negligible for high multiples ( $\ell > r/\Delta r \simeq 1500$ ), this would increase the signal-to-noise ratios by a factor of  $\sim 10$ .

Our results show that studies of the 21-cm bispectrum have the potential to test the gravitational instability scenario and the origin of primordial fluctuations. Measurements of three-point statistics will also provide information on the cosmological parameters through the shape dependence of  $B_{\ell_1\ell_2\ell_3}$  and the redshift evolution of the growth factors.

Low-frequency radio observations with high-angular resolution (a few arcsec, corresponding to  $\ell \sim 10^5$ ) can detect primordial non-Gaussianity with  $f_{\text{NL}} \sim 1$ . One should however take into account that such high values of  $\ell$  correspond to perturbation modes which have crossed the Hubble radius during radiation dominance; for such modes and for values of  $f_{\text{NL}} \sim 1$ , a full second-order evaluation of the matter-transfer function would be needed to account for e.g. the Mészáros effect beyond the linear approximation, following Bartolo, Matarrese & Riotto (2007). On the

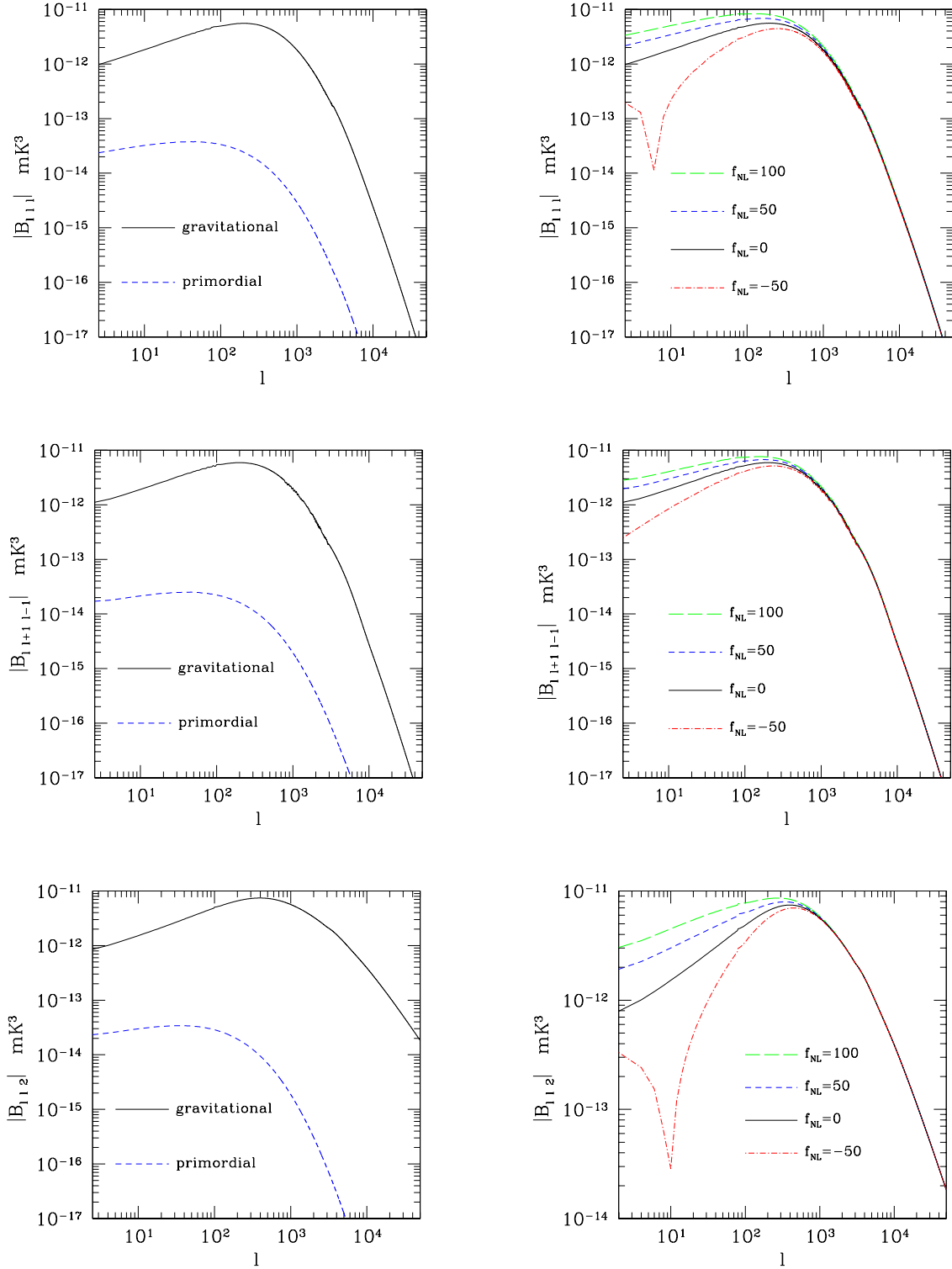


FIG. 2.— The bispectrum of 21-cm anisotropies  $B_{\ell_1, \ell_2, \ell_3}$  measured by an ideal experiment with 0.1 MHz bandwidth centered around  $z = 50$ . From top to bottom, we consider equilateral ( $\ell_1 = \ell_2 = \ell_3$ ), quasi-equilateral ( $\ell_2 = \ell_1 + 1, \ell_2 = \ell_1 - 1$ ) and “squeezed” ( $\ell_2 = \ell_1, \ell_3 = 2$ ) configurations, respectively. In the left panels, the contributions of non-linear gravity (solid) and of primordial non-Gaussianity (with  $f_{\text{NL}} = 1$ ; dashed) are compared. The right panels show the total bispectrum for different values of the non-linearity parameter. Note that in the equilateral and quasi-equilateral configurations the bispectrum vanishes when  $\ell$  is odd (not plotted), is positive for  $\ell = 2j$  with  $j$  an odd integer and negative for  $\ell = 2j$  with  $j$  an even integer.

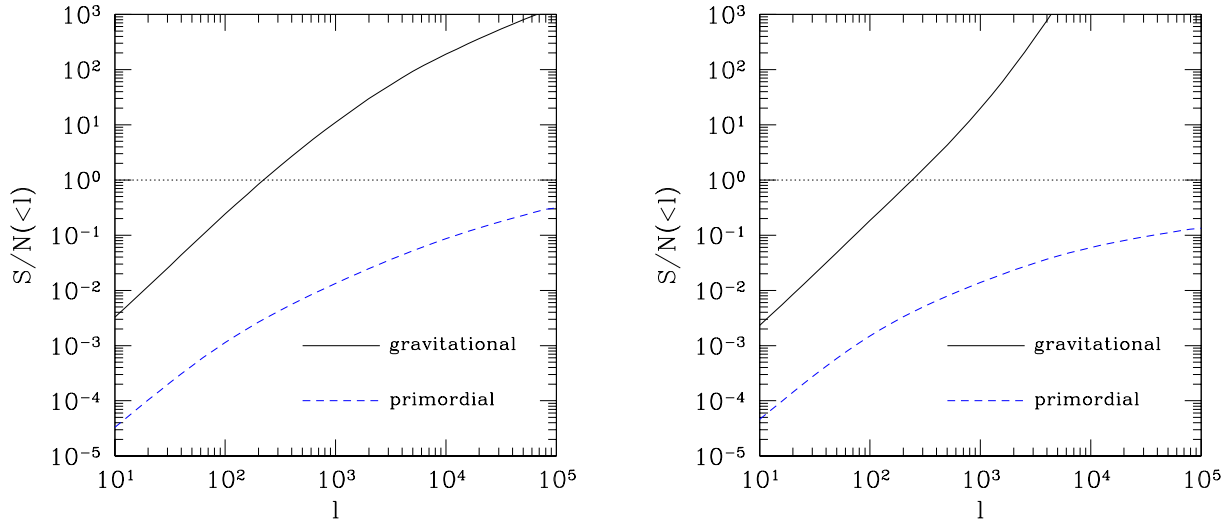


FIG. 3.— Cumulative signal-to-noise ratio for the measurement of the bispectrum of 21-cm anisotropies using modes up to a maximum value of  $\ell$ . Solid lines refer to non-Gaussianity generated by gravity while dashed lines indicate the primordial signal with  $f_{\text{NL}} = 1$ . These quantities have been computed using the signal-to-noise ratio per mode of the quasi-equilateral configuration (left) and of the squeezed configuration (right).

scales of interest, weak lensing by the large-scale structure of the Universe typically modifies the angular power spectrum of 21-cm fluctuations by only  $\sim 1\%$  (Mandel & Zaldarriaga 2006). However, it also produces a non-vanishing disconnected four-point function which represents an additional source of noise for the bispectrum. Potentially this could severely hamper the measurement of  $f_{\text{NL}}$  and a detailed study of the effect is required. Major improvements in the measurement of  $f_{\text{NL}}$  could be achieved by constructing optimal estimators that weigh more those triangular configurations that correspond to particularly high signal-to-noise ratios. We will address these issues in future work.

We thank Nicola Bartolo, Michele Liguori, Simon J. Lilly and Padelis Papadopoulos for helpful discussions. AP thanks the organizers of the workshop on non-Gaussianity held on July 2006 in Trieste where the main results of this paper have been presented.

## REFERENCES

- Acquaviva, V., Bartolo, N., Matarrese S., & Riotto, A., 2003, Nucl. Phys. B, 667, 119  
 Bartolo, N., Komatsu, E., Matarrese S. & Riotto, A., 2004, Phys. Rept., 402, 103  
 Bartolo, N., Matarrese S. & Riotto, A., 2005, JCAP, 0510, 010  
 Bartolo, N., Matarrese S. & Riotto A., 2007, JCAP, 0701, 019  
 Bharadwaj, S. & Ali, S.S. 2004, MNRAS, 352, 142  
 Cooray, A. 2005, MNRAS, 363, 1049  
 Field, G.B. 1958, Proc. Inst. Radio Eng. 46, 240  
 Field, G.B. 1959a, ApJ, 129, 525  
 Field, G.B. 1959b, ApJ, 129, 551  
 Fry, J.N. 1984, ApJ, 279, 499  
 Gangui, A., Lucchin, F., Matarrese, S. & Mollerach, S. 1994, ApJ, 430, 447  
 Kassim, N.E., Perley, R.A., Erickson, W.C., Dwarakanath, K.S. 1993, AJ, 106, 22118  
 Komatsu, E., & Spergel, D. N. 2001, Phys. Rev. D, 63, 063002  
 Loeb, A., & Barkana, R. 2001, ARA&A, 39, 19  
 Loeb, A. & Zaldarriaga, M. 2004, Phys. Rev. Lett., 92, 211301  
 Luo, X., 1994, ApJ, 427, L71  
 Madau, P., Meiksin, A. & Rees, M.J. 1997, ApJ, 475, 429  
 Maldacena, J., 2003, JHEP, 0305, 013  
 Mandel K.S. & Zaldarriaga, M. 2006, ApJ 647, 719  
 Peebles, P. J. E. 1993, Physical Cosmology, Princeton Series in Physics, Princeton, NJ: Princeton University Press  
 Salopek, D.S. & Bond, J.R. 1990, Phys. Rev. D, 42, 3936  
 Salopek, D.S. & Bond, J.R. 1991, Phys. Rev. D, 43, 1500  
 Saiyad, A., Bharadwaj, S. & Pandey, S.K. 2006, MNRAS, 366, 213  
 Scoccimarro, R., Sefusatti, E. & Zaldarriaga, M. 2004, Phys. Rev. D, 69, 103513  
 Scott, D. & Rees, M.J. 1990, MNRAS, 247, 510  
 Seager, S., Sasselov, D. D., & Scott, D. 2000, ApJS, 128, 407  
 Sobolev, V. V. 1960, Moving envelopes of stars, Cambridge: Harvard University Press  
 Spergel, D.N. & Goldberg, D.M., 1999, Phys. Rev. D., 59, 103001  
 Spergel, D. N., et al. 2006, astro-ph/0603449  
 Verde, L., Wang, L.M., Heavens, A. & Kamionkowski, M., 2000a, MNRAS, 313, L141  
 Verde, L., Heavens, A.F. & Matarrese, S., 2000b, MNRAS, 318, 584  
 Verde, L., Jimenez, R., Kamionkowski, M. & Matarrese, S., 2001, MNRAS, 325, 412  
 Weymann, R. 1965, Phys. Fluids, 8, 2112  
 Wouthuysen, S. A. 1952, AJ, 57, 31  
 Zygelman, B. 2005, ApJ, 622, 1356

## APPENDIX

### A. PERTURBATIONS IN THE GAS TEMPERATURE AS A FUNCTION OF DENSITY FLUCTUATIONS

Equation 16 shows that temperature and density perturbations in the cosmic distributions of baryons are related to each other. In this Appendix we want to express  $\delta_T$  in terms of  $\delta$  up to second order in perturbation theory. Our

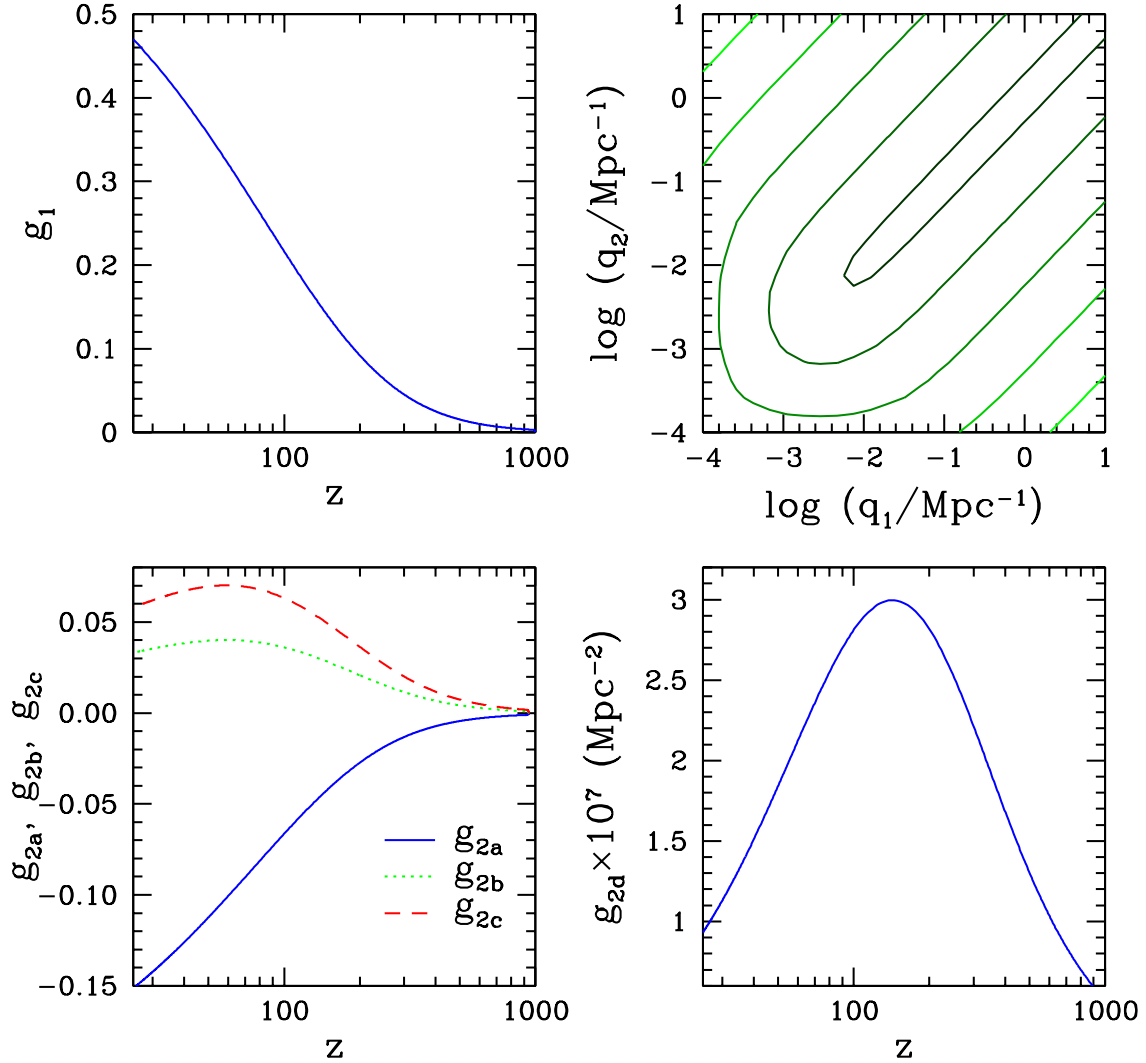


FIG. 4.— Redshift evolution and Fourier-space dependence of the kernels  $\tilde{\mathcal{G}}_1$  and  $\tilde{\mathcal{G}}_2$  relating temperature and density perturbations (see §2.4 and Appendix A for further details). Top left: redshift evolution of the first-order function  $g_1(z)$ . Top right: contour levels of the kernel  $\tilde{\mathcal{G}}_2(\mathbf{q}_1, \mathbf{q}_2, z)$  at  $z = 50$  with  $f_{\text{NL}} = 1$  and  $\mathbf{q}_1 \parallel \mathbf{q}_2$ ; consecutive levels increase by a factor of 10 starting from 0.1 at the centre. Bottom left: redshift evolution of the functions  $g_{2a}, g_{2b}$  and  $g_{2c}$  introduced in equation (A6). Bottom right: redshift evolution of the function  $g_{2d}$  defined in equation (A6).

starting point is the functional expansion given in equation (15) that we Fourier transform, to obtain:

$$\tilde{\delta}_T(\mathbf{k}, t) = \tilde{\mathcal{G}}_1(\mathbf{k}, t) \tilde{\delta}(\mathbf{k}, t) + \int d^3\mathbf{q}_1 \int d^3\mathbf{q}_2 \tilde{\mathcal{G}}_2(\mathbf{q}_1, \mathbf{q}_2, t) \delta_{\text{D}}(\mathbf{q}_1 + \mathbf{q}_2 - \mathbf{k}) \tilde{\delta}(\mathbf{q}_1, t) \tilde{\delta}(\mathbf{q}_2, t) + \dots \quad (\text{A1})$$

Performing a perturbative expansion up to second order gives:

$$\tilde{\delta}_T^{(1)}(\mathbf{k}, t) = \tilde{\mathcal{G}}_1(\mathbf{k}, t) \tilde{\delta}^{(1)}(\mathbf{k}, t), \quad (\text{A2})$$

$$\frac{1}{2} \tilde{\delta}_T^{(2)}(\mathbf{k}, t) = \frac{1}{2} \tilde{\mathcal{G}}_1(\mathbf{k}, t) \tilde{\delta}^{(2)}(\mathbf{k}, t) + \int d^3\mathbf{q} \tilde{\mathcal{G}}_2(\mathbf{q}, \mathbf{k} - \mathbf{q}, t) \tilde{\delta}^{(1)}(\mathbf{q}, t) \tilde{\delta}^{(1)}(\mathbf{k} - \mathbf{q}, t). \quad (\text{A3})$$

Thus, Taylor expanding equation (16) and comparing terms of first perturbative order, one obtains:

$$D_+(t) \frac{\partial \tilde{\mathcal{G}}_1(\mathbf{k}, t)}{\partial t} = -C(t) D_+(t) \tilde{\mathcal{G}}_1(\mathbf{k}, t) + \left( \frac{2}{3} - \tilde{\mathcal{G}}_1(\mathbf{k}, t) \right) \frac{\partial D_+(t)}{\partial t}, \quad (\text{A4})$$

where we factorized the growth of linear overdensities as in equation (25). Since this differential equation does not depend on  $\mathbf{k}$  explicitly, it follows that  $\tilde{\mathcal{G}}_1$  is only a function of time, i.e.  $\tilde{\mathcal{G}}_1(\mathbf{k}, t) = g_1(t)$  and  $\mathcal{G}_1(\mathbf{x}, t) = g_1(t) \delta_{\text{D}}(\mathbf{x})$ .

The corresponding function  $g_1(z)$  can be obtained performing a simple numerical integration and is plotted in Figure 4.

The evolution equation for second-order fluctuations reads

$$\begin{aligned} D_+^2(t) \frac{\partial \tilde{\mathcal{G}}_2(\mathbf{q}_1, \mathbf{q}_2, t)}{\partial t} + \left( 2D_+(t) \frac{\partial D_+(t)}{\partial t} + C(t) D_+^2(t) \right) \tilde{\mathcal{G}}_2(\mathbf{q}_1, \mathbf{q}_2, t) \\ = \left[ \left( \frac{2}{3} - g_1 \right) 2D_+(t) \frac{\partial D_+(t)}{\partial t} - \left( \frac{\partial g_1}{\partial t} + g_1 C(t) \right) D_+^2(t) \right] \mathcal{K}(\mathbf{q}_1, \mathbf{q}_2, t) \\ + \left( \frac{2}{3} g_1 - g_1 \right) 2D_+(t) \frac{\partial D_+(t)}{\partial t} - \left( + \frac{\partial g_1}{\partial t} - g_1 C(t) \right), \end{aligned} \quad (\text{A5})$$

where we used equations (26), (27), (29), and (30) to write  $\tilde{\delta}^{(2)}$  in terms of the kernel  $\mathcal{K}(\mathbf{q}_1, \mathbf{q}_2, t)$ . The solution of this differential equation can be written as follows:

$$\begin{aligned} \tilde{\mathcal{G}}_2(\mathbf{q}_1, \mathbf{q}_2, t) = g_{2a}(t) + g_{2b}(t) \cos^2 \theta_{12} + g_{2c}(t) \left( \frac{q_1}{q_2} + \frac{q_2}{q_1} \right) \cos \theta_{12} \\ + f_{\text{NL}} g_{2d}(t) \frac{T(|\mathbf{q}_1 + \mathbf{q}_2|)}{T(q_1) T(q_2)} \left( \frac{1}{q_1^2} + \frac{1}{q_2^2} + \frac{2}{q_1 q_2} \cos \theta_{12} \right), \end{aligned} \quad (\text{A6})$$

where  $\cos \theta_{12} = \hat{\mathbf{q}}_1 \cdot \hat{\mathbf{q}}_2$ . The time-dependent terms  $g_{2a}, g_{2b}, g_{2c}$  and  $g_{2d}$  are plotted in Figure 4 as a function of redshift.

## B. SECOND ORDER EXPANSION OF $T_{21}$

We present the most general expansion of  $T_{21}$  in terms of all the possible sources of spatial fluctuations up to second order. The brightness temperature of the 21-cm background can be written as:

$$T_{21} = T_{21}^{(0)} + \delta T_{21}^{(1)} + \frac{1}{2} \delta T_{21}^{(2)} \quad (\text{B1})$$

where

$$T_{21}^{(0)} = f_0 \left( 1 - \frac{T_{\text{CMB}}}{\mathcal{S}} \right) (1 - \bar{x}); \quad (\text{B2})$$

$$\delta T_{21}^{(1)} = f_1^{\text{b}} \delta^{(1)} + f_1^{\text{T}} \delta_{\text{T}}^{(1)} + f_1^{\text{x}} \delta_x^{(1)} + f_1^{\text{v}} \frac{\partial v^{(1)}}{\partial r} + f_1^{\alpha} \delta_{\alpha}^{(1)}; \quad (\text{B3})$$

$$\begin{aligned} \frac{1}{2} \delta T_{21}^{(2)} = \frac{1}{2} f_1^{\text{b}} \delta^{(2)} + \frac{1}{2} f_1^{\text{T}} \delta_{\text{T}}^{(2)} + \frac{1}{2} f_1^{\text{x}} \delta_x^{(2)} + \frac{1}{2} f_1^{\text{v}} \frac{\partial v^{(2)}}{\partial r} + \frac{1}{2} f_1^{\alpha} \delta_{\alpha}^{(2)} \\ + f_2^{\text{bb}} \delta^{(1)} \delta^{(1)} + f_2^{\text{TT}} \delta_{\text{T}}^{(1)} \delta_{\text{T}}^{(1)} + f_2^{\text{xx}} \delta_x^{(1)} \delta_x^{(1)} + f_2^{\text{vv}} \frac{\partial v^{(1)}}{\partial r} \frac{\partial v^{(1)}}{\partial r} + f_2^{\alpha\alpha} \delta_{\alpha}^{(1)} \delta_{\alpha}^{(1)} + \\ + f_2^{\text{bx}} \delta^{(1)} \delta_x^{(1)} + f_2^{\text{bT}} \delta^{(1)} \delta_{\text{T}}^{(1)} + f_2^{\text{bv}} \delta^{(1)} \frac{\partial v^{(1)}}{\partial r} + f_2^{\text{b}\alpha} \delta^{(1)} \delta_{\alpha}^{(1)} + \\ + f_2^{\text{Tx}} \delta_{\text{T}}^{(1)} \delta_x^{(1)} + f_2^{\text{Tv}} \delta_{\text{T}}^{(1)} \frac{\partial v^{(1)}}{\partial r} + f_2^{\text{T}\alpha} \delta_{\text{T}}^{(1)} \delta_{\alpha}^{(1)} + \\ + f_2^{\text{xv}} \delta_x^{(1)} \frac{\partial v^{(1)}}{\partial r} + f_2^{\text{x}\alpha} \delta_x^{(1)} \delta_{\alpha}^{(1)} + f_2^{\text{v}\alpha} \frac{\partial v^{(1)}}{\partial r} \delta_{\alpha}^{(1)}. \end{aligned} \quad (\text{B4})$$

Here  $\delta_i^{(n)}$  indicates the  $n$ -th order fluctuation in a given random field denoted by the subscript  $i$ : b stands for the baryon density, T for the gas temperature,  $x$  for the hydrogen ionization fraction, v for the radial peculiar velocity, and  $\alpha$  for the Ly $\alpha$  pumping efficiency.

To simplify the notation, we denote zero-th order (i.e. unperturbed), time-dependent quantities with overlined symbols and we indicate particular combinations of these zero-th order quantities with a few special characters:

$$\mathcal{C} = \frac{4 \kappa_{10}(\bar{T}_{\text{gas}}) T_*}{3 A_{10} \bar{T}_{\text{gas}}} \bar{n}_{\text{HI}}^0, \quad \mathcal{Y}_{\text{C}} = \mathcal{C}(1+z)^3(1-\bar{x}), \quad \mathcal{Y} = 1 + \bar{Y}_{\alpha} + \mathcal{Y}_{\text{C}}, \quad (\text{B5})$$

$$\Delta \mathcal{T} = T_{\text{CMB}} - \bar{T}_{\text{gas}}, \quad \mathcal{S} = \frac{1}{\mathcal{Y}} [T_{\text{CMB}} + \bar{Y}_{\alpha} \bar{T}_{\text{gas}} + \mathcal{Y}_{\text{C}} \bar{T}_{\text{gas}}]. \quad (\text{B6})$$

We also introduce the symbols  $\eta_1$  and  $\eta_2$  to parameterize the dependence of the collisional coupling rate  $\kappa_{10}$  (defined in Section 2.2) up to second order on  $T_{\text{gas}}$ :

$$\kappa_{10} = \kappa_{10}(\bar{T}_{\text{gas}}) \left( \eta_1 \delta_{\text{T}}^{(1)} + \frac{1}{2} \eta_1 \delta_{\text{T}}^{(2)} + \frac{1}{2} \eta_2 \delta_{\text{T}}^{(1)} \delta_{\text{T}}^{(1)} \right). \quad (\text{B7})$$

Adopting this notation, the redshift-dependent weights which couple the brightness temperature to the various sources of fluctuations are:

$$f_0 = \left( \frac{3c^3 \hbar A_{10}}{16k_B \nu_{21}} \right) \frac{\bar{n}_{\text{HI}}}{H_0} \left( \frac{1}{\Omega_m} \right)^{1/2} (1+z)^{1/2} \quad (\text{B8})$$

$$f_1^{\text{b}} = f_0 \left[ \left( 1 - \frac{T_{\text{CMB}}}{\mathcal{S}} \right) (1 - \bar{x}) - \frac{T_{\text{CMB}} \mathcal{C} (1+z)^3}{\mathcal{Y}^2 \mathcal{S}^2} \Delta \mathcal{T} (1 - \bar{x})^2 \right] \quad (\text{B9})$$

$$f_1^{\text{T}} = f_0 \left[ \frac{T_{\text{CMB}} \mathcal{C} (1+z)^3}{\mathcal{Y} \mathcal{S}} \left( 1 - 2 \frac{\Delta \mathcal{T}}{\mathcal{Y} \mathcal{S}} \eta_1 \right) (1 - \bar{x})^2 + \frac{T_{\text{CMB}}}{\mathcal{Y} \mathcal{S}^2} (\bar{Y}_\alpha \bar{T}_{\text{gas}}) (1 - \bar{x}) \right] \quad (\text{B10})$$

$$f_1^{\text{x}} = f_0 \left[ - \left( 1 - \frac{T_{\text{CMB}}}{\mathcal{S}} \right) \bar{x} + \frac{T_{\text{CMB}} \mathcal{C} (1+z)^3}{\mathcal{Y}^2 \mathcal{S}^2} \Delta \mathcal{T} (1 - \bar{x}) \bar{x} \right] \quad (\text{B11})$$

$$f_1^{\text{v}} = f_0 \left[ - \left( 1 - \frac{T_{\text{CMB}}}{\mathcal{S}} \right) (1 - \bar{x}) \frac{1+z}{H} \right] \quad (\text{B12})$$

$$f_1^{\alpha} = f_0 \left[ - \frac{\bar{Y}_\alpha}{\mathcal{Y}^2 \mathcal{S}^2} \Delta \mathcal{T} T_{\text{CMB}} (1 - \bar{x}) \right] \quad (\text{B13})$$

$$f_2^{\text{bb}} = f_0 \left[ - \frac{T_{\text{CMB}} \mathcal{C} (1+z)^3}{\mathcal{Y}^2 \mathcal{S}^2} \Delta \mathcal{T} (1 - \bar{x})^2 + \frac{T_{\text{CMB}} \mathcal{C}^2 (1+z)^6}{\mathcal{S}^2 \mathcal{Y}^3} \Delta \mathcal{T} \left( 1 - \frac{\delta \mathcal{T}}{\mathcal{S} \mathcal{Y}} \right) (1 - \bar{x})^3 \right] \quad (\text{B14})$$

$$\begin{aligned} f_2^{\text{TT}} = f_0 & \left[ \frac{T_{\text{CMB}} \mathcal{C} (1+z)^3}{\mathcal{Y} \mathcal{S}} \left( 1 - \eta_1 + \frac{\Delta \mathcal{T}}{\mathcal{Y} \mathcal{S}} \eta_2 (1 - \bar{x})^2 \right) + \right. \\ & - \frac{T_{\text{CMB}} \mathcal{C} (1+z)^3}{\mathcal{Y}^2 \mathcal{S}^2} (\bar{Y}_\alpha \bar{T}_{\text{gas}}) \left( 1 + \eta_1 \left( 1 - 4 \frac{\Delta \mathcal{T}}{\mathcal{Y} \mathcal{S}} \right) \right) (1 - \bar{x})^2 + \\ & + \frac{T_{\text{CMB}} \mathcal{C}^2 (1+z)^6}{\mathcal{S} \mathcal{Y}^2} \left( -2 + 4 \left( \frac{\Delta \mathcal{T}}{\mathcal{S} \mathcal{Y}} \right) + \left( 1 - 4 \left( \frac{\Delta \mathcal{T}}{\mathcal{S} \mathcal{Y}} \right)^2 \right) \eta_1 \right) (1 - \bar{x})^3 + \\ & \left. - \frac{T_{\text{CMB}}}{\mathcal{Y}^3 \mathcal{S}^2} (\bar{Y}_\alpha \bar{T}_{\text{gas}})^2 (1 - \bar{x}) \right] \quad (\text{B15}) \end{aligned}$$

$$f_2^{\text{xx}} = f_0 \left[ + \frac{T_{\text{CMB}} \mathcal{C} (1+z)^3}{\mathcal{Y}^2 \mathcal{S}^2} \Delta \mathcal{T} \bar{x}^2 - \frac{T_{\text{CMB}} \mathcal{C}^2 (1+z)^6}{\mathcal{Y}^3 \mathcal{S}^2} \Delta \mathcal{T} \left( 1 - \frac{\Delta \mathcal{T}}{\mathcal{Y} \mathcal{S}} \right) (1 - \bar{x}) \bar{x}^2 \right] \quad (\text{B16})$$

$$f_2^{\text{vv}} = f_0 \left[ \left( 1 - \frac{T_{\text{CMB}}}{\mathcal{S}} \right) (1 - \bar{x}) \frac{(1+z)^2}{H^2} \right] \quad (\text{B17})$$

$$f_2^{\alpha\alpha} = f_0 \left[ + \frac{\bar{Y}_\alpha}{\mathcal{Y}^3 \mathcal{S}^2} \Delta \mathcal{T} T_{\text{CMB}} \left( 1 - \frac{\bar{Y}_\alpha}{\mathcal{Y} \mathcal{S}} \Delta \mathcal{T} \right) (1 - \bar{x}) \right] \quad (\text{B18})$$

$$\begin{aligned} f_2^{\text{bT}} = f_0 & \left[ \frac{T_{\text{CMB}} \mathcal{C} (1+z)^3}{\mathcal{Y} \mathcal{S}} \left( 2 - 3 \left( \frac{\Delta \mathcal{T}}{\mathcal{Y} \mathcal{S}} \right) \eta_1 \right) (1 - \bar{x})^2 + \right. \\ & - \frac{T_{\text{CMB}} \mathcal{C} (1+z)^3}{\mathcal{Y}^2 \mathcal{S}^2} (\bar{Y}_\alpha \bar{T}_{\text{gas}}) \left( 1 - 2 \frac{\Delta \mathcal{T}}{\mathcal{S} \mathcal{Y}} \right) (1 - \bar{x})^2 + \frac{T_{\text{CMB}}}{\mathcal{Y} \mathcal{S}^2} (\bar{Y}_\alpha \bar{T}_{\text{gas}}) (1 - \bar{x}) + \\ & \left. + \frac{T_{\text{CMB}} \mathcal{C}^2 (1+z)^6}{\mathcal{Y}^2 \mathcal{S}} \left( -2 + \frac{\bar{T}_{\text{gas}}}{\mathcal{S}} + 2 \frac{\Delta \mathcal{T}}{\mathcal{Y} \mathcal{S}} (1 + \eta_1) - 4 \left( \frac{\Delta \mathcal{T}}{\mathcal{Y} \mathcal{S}} \right)^2 \eta_1 \right) (1 - \bar{x})^3 \right] \quad (\text{B19}) \end{aligned}$$

$$f_2^{\text{bx}} = f_0 \left[ - \left( 1 - \frac{T_{\text{CMB}}}{\mathcal{S}} \right) \bar{x} + 3 \frac{T_{\text{CMB}} \mathcal{C} (1+z)^3}{\mathcal{Y}^2 \mathcal{S}^2} \Delta \mathcal{T} (1-\bar{x}) \bar{x} + \right. \\ \left. - 2 \frac{T_{\text{CMB}} \mathcal{C}^2 (1+z)^6}{\mathcal{Y}^3 \mathcal{S}^2} \Delta \mathcal{T} \left( 1 - \frac{\Delta \mathcal{T}}{\mathcal{Y} \mathcal{S}} \right) (1-\bar{x})^2 \bar{x} \right] \quad (\text{B20})$$

$$f_2^{\text{bv}} = f_0 \left[ - \left( 1 - \frac{T_{\text{CMB}}}{\mathcal{S}} \right) (1-\bar{x}) \frac{1+z}{H} + \frac{T_{\text{CMB}} \mathcal{C} (1+z)^3}{\mathcal{Y}^2 \mathcal{S}^2} \Delta \mathcal{T} (1-\bar{x})^2 \frac{1+z}{H} \right] \quad (\text{B21})$$

$$f_2^{\text{b}\alpha} = f_0 \left[ - 2 \frac{T_{\text{CMB}} \mathcal{C} (1+z)^3}{\mathcal{Y}^2 \mathcal{S}^2} \left( \bar{Y}_\alpha \bar{T}_{\text{gas}} + \frac{\bar{Y}_\alpha}{\mathcal{Y}^2 \mathcal{S}} \Delta \mathcal{T}^2 \right) (1-\bar{x})^2 - \frac{\bar{Y}_\alpha}{\mathcal{Y}^2 \mathcal{S}^2} \Delta \mathcal{T} T_{\text{CMB}} (1-\bar{x}) \right] \quad (\text{B22})$$

$$f_2^{\text{T}x} = f_0 \left[ - \frac{T_{\text{CMB}} \mathcal{C} (1+z)^3}{\mathcal{Y} \mathcal{S}} \left( 2 - 3 \left( \frac{\Delta \mathcal{T}}{\mathcal{Y} \mathcal{S}} \right) \eta_1 \right) (1-\bar{x}) \bar{x} + \right. \\ \left. + \frac{T_{\text{CMB}} \mathcal{C} (1+z)^3}{\mathcal{Y}^2 \mathcal{S}^2} (\bar{Y}_\alpha \bar{T}_{\text{gas}}) \left( 1 - 2 \frac{\Delta \mathcal{T}}{\mathcal{S} \mathcal{Y}} \right) (1-\bar{x}) \bar{x} - \frac{T_{\text{CMB}}}{\mathcal{Y} \mathcal{S}^2} (\bar{Y}_\alpha \bar{T}_{\text{gas}}) \bar{x} + \right. \\ \left. - \frac{T_{\text{CMB}} \mathcal{C}^2 (1+z)^6}{\mathcal{Y}^2 \mathcal{S}} \left( - 2 + \frac{\bar{T}_{\text{gas}}}{\mathcal{S}} + 2 \frac{\Delta \mathcal{T}}{\mathcal{Y} \mathcal{S}} (1 + \eta_1) - 4 \left( \frac{\Delta \mathcal{T}}{\mathcal{Y} \mathcal{S}} \right)^2 \eta_1 \right) (1-\bar{x})^2 \bar{x} \right] \quad (\text{B23})$$

$$f_2^{\text{T}v} = f_0 \left[ + 2 \frac{T_{\text{CMB}} \mathcal{C} (1+z)^3}{\mathcal{Y}^2 \mathcal{S}^2} \Delta \mathcal{T} (1-\bar{x}) \eta_1 \frac{1+z}{H} - \frac{T_{\text{CMB}} \mathcal{C} (1+z)^3}{\mathcal{Y}^2 \mathcal{S}^2} (\mathcal{Y} \mathcal{S}) (1-\bar{x})^2 \frac{1+z}{H} + \right. \\ \left. - \frac{\bar{Y}_\alpha}{\mathcal{Y} \mathcal{S}^2} T_{\text{CMB}} \bar{T}_{\text{gas}} (1-\bar{x}) \frac{1+z}{H} \right] \quad (\text{B24})$$

$$f_2^{\text{T}\alpha} = f_0 \left[ \frac{T_{\text{CMB}} \mathcal{C} (1+z)^3}{\mathcal{Y}^2 \mathcal{S}^2} (\bar{Y}_\alpha \bar{T}_{\text{gas}}) (1-2\eta_1) (1-\bar{x})^2 \eta_1 + \frac{\bar{Y}_\alpha}{\mathcal{Y}^2 \mathcal{S}^2} \bar{T}_{\text{gas}} T_{\text{CMB}} \left( 1 - \frac{\bar{Y}_\alpha}{\mathcal{Y}} \right) + \right. \\ \left. + 2 \frac{T_{\text{CMB}} \mathcal{C} (1+z)^3}{\mathcal{Y} \mathcal{S}^2} \frac{\bar{Y}_\alpha}{\mathcal{Y}^2} \Delta \mathcal{T} \left( 1 - 2 \left( \frac{\Delta \mathcal{T}}{\mathcal{Y} \mathcal{S}} \right) \eta_1 \right) (1-\bar{x})^2 + 2 \frac{\bar{Y}_\alpha}{\mathcal{Y}^3 \mathcal{S}^3} \bar{T}_{\text{gas}} \Delta \mathcal{T} T_{\text{CMB}} (1-\bar{x}) \right] \quad (\text{B25})$$

$$f_2^{\text{x}v} = f_0 \left[ \left( 1 - \frac{T_{\text{CMB}}}{\mathcal{S}} \right) \bar{x} \frac{1+z}{H} - \frac{T_{\text{CMB}} \mathcal{C} (1+z)^3}{\mathcal{Y}^2 \mathcal{S}^2} \Delta \mathcal{T} (1-\bar{x}) \bar{x} \frac{1+z}{H} \right]. \quad (\text{B26})$$

$$f_2^{\text{x}\alpha} = f_0 \left[ + 2 \frac{T_{\text{CMB}} \mathcal{C} (1+z)^3}{\mathcal{Y}^2 \mathcal{S}^2} \left( (\bar{Y}_\alpha \bar{T}_{\text{gas}}) + \frac{\bar{Y}_\alpha}{\mathcal{Y}^2 \mathcal{S}} \Delta \mathcal{T}^2 \right) (1-\bar{x}) \bar{x} + \frac{\bar{Y}_\alpha}{\mathcal{Y}^2 \mathcal{S}^2} \Delta \mathcal{T} T_{\text{CMB}} \bar{x} \right] \quad (\text{B27})$$

$$f_2^{\text{v}\alpha} = f_0 \left[ \frac{\bar{Y}_\alpha}{\mathcal{Y}^2 \mathcal{S}^2} \Delta \mathcal{T} T_{\text{CMB}} (1-\bar{x}) \frac{1+z}{H} \right]. \quad (\text{B28})$$